Available online at www.CivileJournal.org

Civil Engineering Journal

Vol. 2, No. 9, September, 2016

The Effect of Rail Defects on Track Impact Factors

Mohammad Fesharaki[a*], Ton-Lo Wang [a]

[a] *Department of Civil and Environmental Engineering, Florida International University, Miami, USA.*

Received 15 September 2016; Accepted 1 October 2016

Abstract

This paper investigates the effect of rail surface flaws on track impact factors for different track and vehicle conditions. For this purpose, a three dimensional vehicle and track as an integrated system modelled. The vehicle, consists car body, bogie frames and wheelsets, is able to model displacements in vertical and lateral directions. Hertz nonlinear springs utilized to connect vehicle to track structure and simulate the interaction between vehicle and track subsystems. Track comprises rail, rail pads, sleepers and ballast materials. For each subsystem, matrices of mass, stiffness and damping were formed and then matrices of total vehicle-track system considering their interaction were solved. Using FRA spectral density functions for rail irregularities, response of track with different qualities to train dynamic forces obtained. Rail random irregularities, rail corrugation and rail joint defects as three common rail defects have been considered in this paper. For each defects the influence of different track and train parameters on impact factor has been studied. The results of study indicate substantial effect of the depth and frequency of the rail flaws on impact factors. This paper has also considered the impact of vehicle speed on dynamic forces and found the critical speed for each case.

Keywords: High-Speed Rail; Vibration; Rail Defect; Impact Factor.

1. Introduction

Rail surface defects not only damage the wheels and vehicle but also cause a considerable increase in dynamics loads and expedite the deterioration rate of railroad track. It is also shown that rail defects including broken rail are the main reason of rail accidents. Based on the results of an analysis of causes of major train derailment conducted by Liu et al. [1], rail defects accounted for almost 20% of all derailments and more than 30% of all derailed cars on class I main lines. Therefore, Rail defects have always been a matter of concern and investigated by many researchers [2-4]. Since the conventional theoretical model cannot properly predict track behavior [5], more realistic three dimensional models developed for track analysis. Sun and Dhanasekar [6] using a 3D vehicle-track model and considering periodic and impulsive defects concluded that periodic defect is more serious than the impulse excitation and the impulse excitation produces much higher impact forces. Kabo et al. [7], carried out numerical analyses of high-frequency dynamic train–track interaction which is combined with the analysis of material deterioration in terms of rolling contact fatigue and plastic deformations to analyze the influence of insulated rail joints. The result of the study showed that introduction of an insulated joint alters the dynamic characteristics of the track. This effect and the introduced surface irregularity of the rail cause high contact load a magnitude that increases with increasing train speed. Sun et al. [8] using a rail vehicle-track interaction dynamics model, determined the track vertical dynamic forces due to short wavelength dip defects such as squat, dip joints and welds. The dependence of the track vertical dynamic forces on the rail dip defect size and vehicle speed also investigated. Wu and Thompson [9] theoretically investigated the impact noise generation due to a wheel passing over dipped rail joints. They showed that train speed has a great influence on wheel/rail impact force as well as the level of noise. Jin et al. [10] modeled a three-dimensional train–track interaction system and studied rail corrugation for different conditions. They concluded that the corrugation with high passing frequencies has a great influence on the dynamic performance of the wheelsets and track, but little on the car-body and the bogie frame. It is also shown that under the condition of the same speed and the same wavelength, the deeper the corrugation depth from peak to trough is, the greater the influence on the dynamic performance and the rail material wear are.

* Corresponding author: mfesh001@fiu.edu

The purpose of this paper is to investigate different rail's surface flaws and compare the effect of rail defects for different conditions. For this purpose, a three dimensional train-track integrated model is developed to study rail flaws for different train speeds. The train and track subsystems interact by nonlinear Hertz springs. Rail is modeled as Euler-Bernoulli beam with six degrees of freedom at each node. To model granular materials and their effect on track dynamics, ballast pyramid model is used to take into account the effective mass of ballast on vibration. The vehicle and track can simulate the vertical and lateral response of railroad track. The results of this study prove the significance of flaws characteristics as well as train speed on rail forces and emphasizes that developing rail defects at a certain depth and frequency is very dangerous for high-speed rail and might increase impact factor to 200%.

2. Vehicle model

In this research, vehicle is simulated using a 31-DOF mass–spring–dashpot system including a car body, two bogies and four wheelsets. The mass of each body, bogie frames and wheels are lumped in their centers of gravity. Vehicle bodies are assumed to be rigid and undergo translation and rotation. Car body and bogie frames are characterized by five DOFs in translation in vertical and lateral directions and rotation about x, y and z axis so called rolling, yawing and pitching. Figure 1. shows the schematic model of vehicle.

The secondary suspension system that connects the car-body to bogie frames is characterized by two linear springs and two viscous dashpots in both horizontal and vertical directions. The primary suspension system, linking bogies and wheelsets, is also modeled using linear springs and viscous dashpots. Wheelsets have 4 DOFs in lateral, rolling, yawing and vertical directions. As a result, for a 4-axle vehicle, the total number of DOFs is 31 [11].

Dynamic equations of motion of vehicle's body can be formed using the dynamic equilibrium method or energy methods such as principle of a stationary value of total potential energy of a dynamic system. Vehicle consists of concentrated mass as a result; the vehicle's mass matrix is diagonal and has the following shape:

$$\left[M^{veh}\right]=diag\left[\left[M^{car}\right]\ \left[M^{bog}\right]\ \left[M^{bog}\right]\ \left[M^{whl}\right]\right] \tag{1}$$

Where

$$\left[M^{car}\right]=diag\left[M_c\quad J_{cx}\quad J_{cy}\quad M_c\quad J_{cz}\right]$$

$$\left[M^{bog}\right]=diag\left[M_{bi}\quad J_{bxi}\quad J_{byi}\quad M_{bi}\quad J_{bzi}\right]\ i=1,\ 2$$

$$\left[M^{whl}\right]=diag\left[M_{wi}\quad J_{wxi}\quad J_{wyi}\quad M_{wi}\right]\ i=1\ to\ 4$$

$[M^{car}]$, $[M^{bog}]$ and $[M^{whl}]$, are diagonal matrices representing the mass of car body, bogies and wheelsets. $[M^{veh}]$ is vehicle's total mass matrix. The values of mass and inertia moments of vehicle's bodies are shown in Table 1.

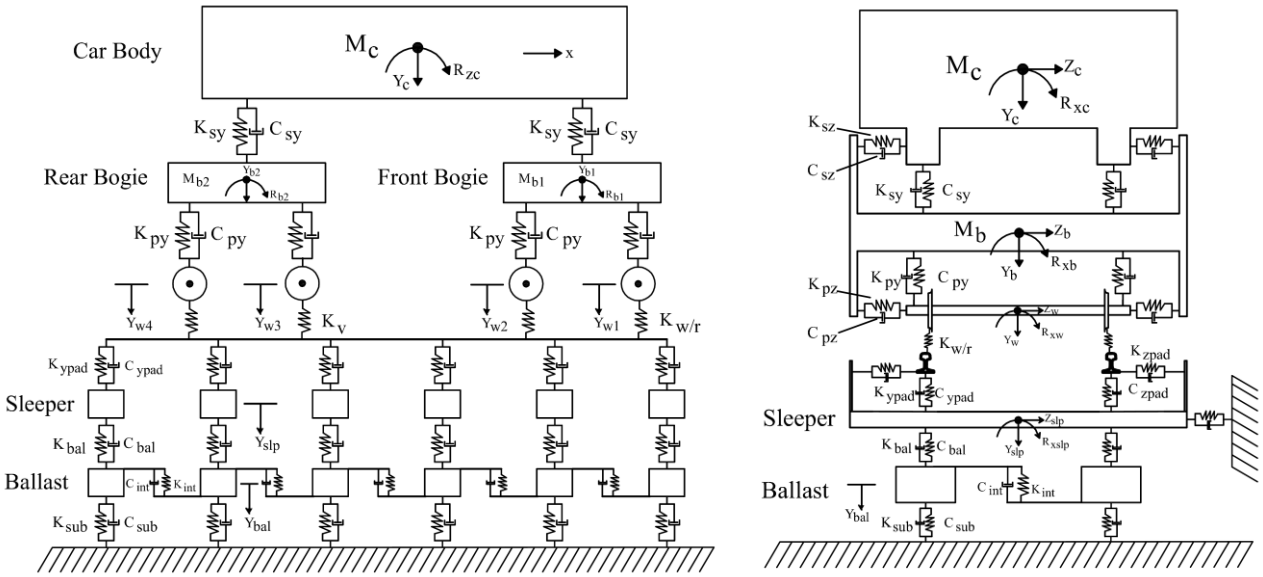

Figure 1. Vehicle model, (left) side view, (right) front view

The stiffness matrix of the vehicle can be obtained by finding the each body's coefficients of displacement. It is a 31×31 symmetric matrix and takes the following form:

$$\left[K^{veh}\right]=\begin{bmatrix} K_c & K_{cb1} & K_{cb2} & 0 & 0 & 0 & 0 \\ & K_{b1} & 0 & K_{b1w1} & K_{b1w2} & 0 & 0 \\ & & K_{b2} & 0 & 0 & K_{b2w3} & K_{b2w4} \\ & & & K_{w1} & 0 & 0 & 0 \\ & & & & K_{w2} & 0 & 0 \\ & & & & & K_{w3} & 0 \\ sym & & & & & & K_{w4} \end{bmatrix} \quad (2)$$

In which K_c, K_b and K_w show the springs connected to car body, bogies and wheelsets. K_{bw} and K_{cb} demonstrate the link between bogies-wheelsets and car body-bogies. $[K^{veh}]$ is the vehicle's total stiffness matrix Having viscous damping coefficients of vehicle's suspension systems, the same procedure can be applied to obtain the damping matrix of vehicle.

The force applied to the vehicle, is either gravity force or wheel-rail interaction force:

$$F_g^v = \left(\frac{1}{4}M_c + \frac{1}{2}M_b + M_w\right)g \quad (3)$$

$$\left[F^{w/r}\right]=\left[F_z^{w/r} \quad M_x^{w/r} \quad M_y^{w/r} \quad F_y^{w/r}\right]^T \quad (4)$$

Where "g" is gravitational acceleration. $F_z^{w/r}, M_x^{w/r}, M_y^{w/r}$ *and* $F_y^{w/r}$ are the lateral contact force, rolling and yawing moments and vertical contact force.

The total equation of motion of vehicle then can be formed:

$$[M^{veh}]\{\ddot{U}^{veh}\} + [C^{veh}]\{\dot{U}^{veh}\} + [K^{veh}]\{U^{veh}\} = \{F^{veh}\} \quad (5)$$

Table 1. Vehicle Parameters

Notation	Parameter	Value	Unit
M_c	Mass of car body	47	ton
$J^c_{x,y,z}$	Car body inertia moments about x, y and z	49.50, 1950 ,2210	Ton.m^2
M_b	Mass of bogie	3.1	ton
$J^b_{x,y,z}$	Bogie inertia moments about x, y and z	1.55, 2.34, 5.1	Ton.m^2
K_{sy}	Vertical stiffness of secondary suspension	2.15×10^5	N/m
K_{sz}	Lateral stiffness of secondary suspension	2.75×10^5	N/m
K_{py}	Vertical stiffness of primary suspension	6.55×10^5	N/m
K_{pz}	Lateral stiffness of primary suspension	2.35×10^6	N/m
M_w	Mass of wheel axle	1.7	ton
$J^w_{x,y,z}$	Wheel axle inertia moments about x, y and z	1.5, 1.2, 0.005	Ton.m^2
L_c	Length of car body	6.3	m
R_{wheel}	Wheel rolling radius	0.5	m
E	Wheel's modulus of elasticity	2×10^{11}	N/ m^2
ν	Wheel's Poisson ratio	0.3	-

3. Train-track interaction

Train and track interact through wheel and rail contact. The interaction force between rail and wheel can be determined by finding the contact area. One model that successfully describes the vehicle-track interaction is Hertz contact theory which states that the elastic deformation of the steel of the wheel and the rail creates an elliptic area. The dimensions of the contact ellipse are determined by the normal force on the area, while the ratio of ellipse axes "a" and "b" depends on the main curvatures of the wheel and rail profiles. Figure 2. shows the contact area between wheel and rail [12].

To find the wheel-rail contact force, the contact stiffness $K_{w/r}$ needs to be defined first which depends on the wheel load and wheel and rail properties:

$$K_{w/r} = \frac{4E\sqrt[4]{R_{wheel}R_{rail}}}{3(1-\nu^2)} \quad (6)$$

Where R_{wheel} and R_{rail} are wheel rolling radius and rail head radius respectively and P is the static wheel load. In Equation 6, it is assumed that wheel and rail have the same modulus of elasticity, E and Poisson ratio, ν.

The wheel-rail contact force $F_{w/r}$ then can be determined by:

$$F_{w/r} = K_{w/r}(y_{wheel} - y_{rail})^{3/2} \quad (7)$$

y_{wheel} and y_{rail} are wheel and rail vertical displacements. The contact force is nonlinear elastic and tensionless which means that if $y_{wheel} - y_{rail}<0$ or wheel and rail are not in contact then the force will be equal to zero. It should be noted that in the above formula, rail irregularities will be added to rail displacement.

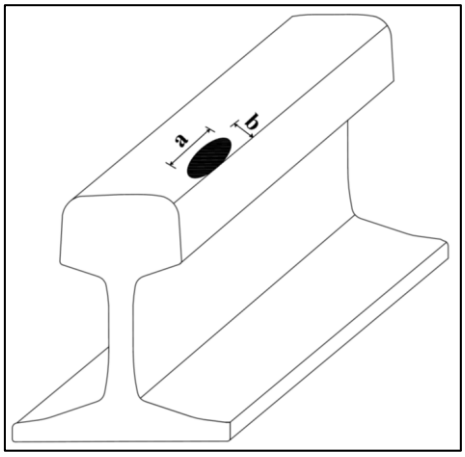

Figure 2. Wheel-rail contact area

4. Rail irregularities

Rail irregularities are deviations of rails from ideal track position. Four types of track irregularity can be distinguished: vertical profile, alignment, cross level and gauge irregularities, which are caused mainly by wear, initial installation errors, degradation of support materials, improper clearances, track settlement, and their combinations [2]. Since rail irregularity is a random process, it is best described by using Power Spectral Density (PSD) functions. Different researchers and railroads have developed PSD functions to describe rail irregularities. FRA (Federal Railway Administration) collected a large database of track irregularities profiles in the United States. Based on recorded rail profiles, FRA defined six classes (1 the worst and 6 best quality) to characterize the roughness of the rail and track quality. FRA suggested the following PSD functions for rail irregularities [13]:

$$S_{e,a}(n) = \frac{An_2^2(n^2 + n_1^2)}{n^4(n^2 + n_2^2)} \quad (8)$$

$$S_{c,g}(n) = \frac{An_2^2}{(n^2 + n_1^2)(n^2 + n_2^2)} \quad (9)$$

Where $S_{e,a}$ is PSD function for vertical profile and alignment and $S_{c,g}$ is the PSD function for cross level and gauge irregularities. A is the roughness parameter (in^2-cycle/ft.). n_1 and n_2 are the break frequencies (cycle/ft.). The values of A, n_1, and n_2 are different for track classes 1 to 6 [13, 14].

By utilizing the spectral representation method, artificial rail irregularity profile can be generated [15]:

$$\varepsilon(x) = \sum_{n=1}^{N} \sqrt{2S(n_n)\Delta n}\cos(2\pi n_n x - \theta_n) \quad (10)$$

Where R_n is a random number between 0 and 1.

$$n_n = n\Delta n = n\frac{n_u - n_l}{N}$$

where N represents the total number of discrete spatial frequencies considered, and n_n is the nth discrete frequency. n_u and n_l are respectively the maximum and minimum frequencies considered and $\theta_n = 2\pi R_n$ is random phase angle where R_n is a random number between 0 and 1.

If R and L refer to right and left rails, then the vertical (u_y) and lateral (u_z) irregularities are given as [14]:

$$u_{yR} = (\varepsilon_v + \frac{1}{2}\varepsilon_c), \quad u_{zR} = (\varepsilon_a + \frac{1}{2}\varepsilon_g), \quad (11)$$

$$u_{yL} = (\varepsilon_v - \frac{1}{2}\varepsilon_c), \quad u_{zL} = (\varepsilon_a - \frac{1}{2}\varepsilon_g), \quad (12)$$

In which ε_v, ε_c, ε_a and ε_g are vertical profile, cross level, alignment and gauge irregularities respectively. Figure 3. shows artificial rail irregularities for track class 6, produced using FRA's PSD functions.

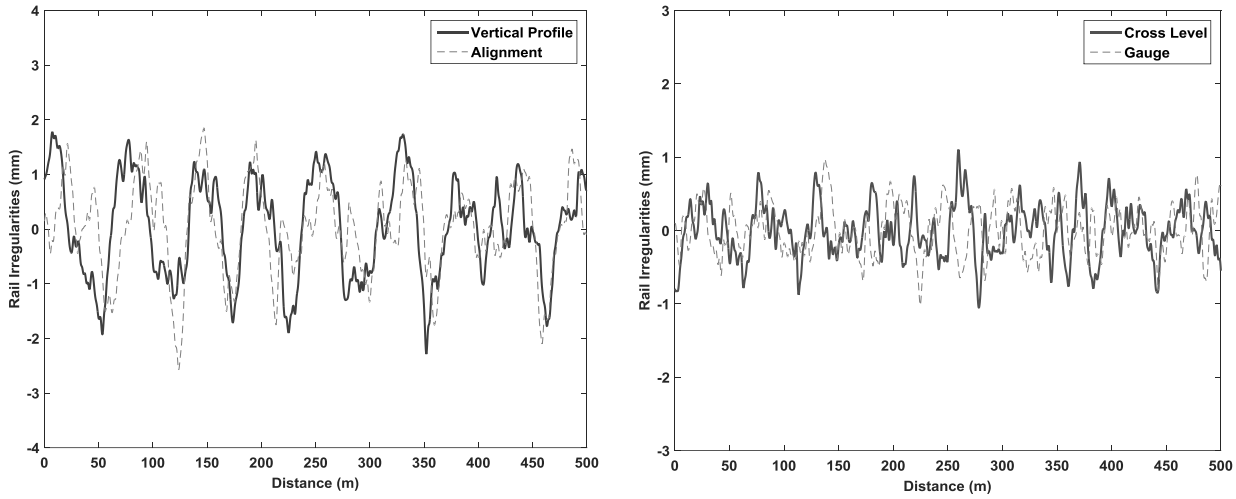

Figure 3. FRA track class 6 rail irregularities, Vertical profile and alignment irregularities (left), Cross level and gauge irregularities (right)

5. Track model

Track model consists of rail, rail pad, sleeper and ballast. Rail is modeled as beam elements with six degrees of freedom at each node. So the nodal displacements of rail can be expressed as a vector:

$$[U] = [u_1 \quad v_1 \quad w_1 \quad \alpha_1 \quad \beta_1 \quad \gamma_1 \quad u_2 \quad v_2 \quad w_2 \quad \alpha_2 \quad \beta_2 \quad \gamma_2]^T \tag{13}$$

Where u, v and w represent displacement in x, y and z directions and α, β and γ denotes rotation around x, y and z axes. Subscripts 1 and 2 indicate first (left) and second (right) node of a beam element [16].

First order Lagrange shape functions (N_1 and N_2) and cubic Hermitian interpolation functions (N_3, N_4, N_5, N_6) are used to describe the axial and flexural deflections of beam elements. Note that 'e' is the distance from the left node of the beam and 'l' is the beam element length. To simplify solution, the length of beam elements are equal to the distance between two adjacent sleepers. Figure 4, shows the beam element and its DOFs.

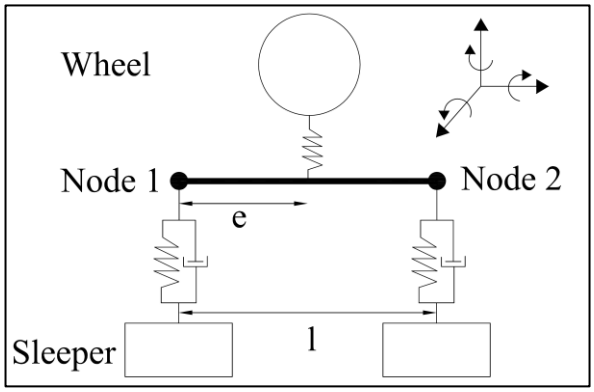

Figure 4. beam element's DOFs

The interpolation vectors for the axial, vertical, lateral, and torsional displacements are given as follows:

$$\begin{aligned}
[N_u] &= [N_1 \quad 0 \quad 0 \quad 0 \quad 0 \quad 0 \quad N_2 \quad 0 \quad 0 \quad 0 \quad 0 \quad 0]^T \\
[N_v] &= [0 \quad N_3 \quad 0 \quad 0 \quad 0 \quad N_4 \quad 0 \quad N_5 \quad 0 \quad 0 \quad 0 \quad N_6]^T \\
[N_w] &= [0 \quad 0 \quad N_3 \quad 0 \quad -N_4 \quad 0 \quad 0 \quad 0 \quad N_5 \quad 0 \quad -N_6 \quad 0]^T \\
[N_\alpha] &= [0 \quad 0 \quad 0 \quad N_1 \quad 0 \quad 0 \quad 0 \quad 0 \quad 0 \quad N_2 \quad 0 \quad 0]^T
\end{aligned} \tag{14}$$

Where:

$$N_1(e) = 1 - \frac{e}{l}$$

$$N_2(e) = \frac{e}{l}$$

$$N_3(e) = 1 - 3\left(\frac{e}{l}\right)^2 + 2\left(\frac{e}{l}\right)^3$$

$$N_4(e) = e\left(1 + \left(\frac{e}{l}\right)^2 - 2\left(\frac{e}{l}\right)\right)$$

$$N_5(e) = 3\left(\frac{e}{l}\right)^2 - 2\left(\frac{e}{l}\right)^3$$

$$N_6(e) = e\left(\left(\frac{e}{l}\right)^2 - \left(\frac{e}{l}\right)\right)$$

The displacements of a rail element can be related to nodal DOFs as follows:

$$\begin{aligned} u(x) &= [N_u][U] \\ v(x) &= [N_v][U] \\ w(x) &= [N_w][U] \\ \alpha(x) &= [N_\alpha][U] \end{aligned} \tag{15}$$

The mass matrix for the beam element can be written in the following form:

$$[M] = \frac{\overline{m}}{420}\begin{bmatrix} 140 & 0 & 0 & 0 & 0 & 0 & 70 & 0 & 0 & 0 & 0 & 0 \\ & 156 & 0 & 0 & 0 & 22l & 0 & 54 & 0 & 0 & 0 & -13l \\ & & 156 & 0 & -22l & 0 & 0 & 0 & 54 & 0 & 13l & 0 \\ & & & 140r^2 & 0 & 0 & 0 & 0 & 0 & 70r^2 & 0 & 0 \\ & & & & 4l^2 & 0 & 0 & 0 & -13l & 0 & -3l^2 & 0 \\ & & & & & 4l^2 & 0 & 13l & 0 & 0 & 0 & -3l^2 \\ & & & & & & 140 & 0 & 0 & 0 & 0 & 0 \\ & & & & & & & 156 & 0 & 0 & 0 & -22l \\ & & & & & & & & 156 & 0 & 22l & 0 \\ & & & & & & & & & 140r^2 & 0 & 0 \\ & & & & & & & & & & 4l^2 & 0 \\ Sym & & & & & & & & & & & 4l^2 \end{bmatrix} \tag{16}$$

The mass matrix of rail is composed of mass matrices of right and left rail then can be expressed as the following formula:

$$M_R = \begin{bmatrix} M_{rr} & 0 \\ 0 & M_{lr} \end{bmatrix} \tag{17}$$

Where M_{rr} and M_{lr} are mass matrix of right and left rail respectively. Since each beam element has 12 degrees of freedom, the total DOFs of mass matrix for right and left rail would be 24.

The same procedure and shape function is utilized to find the stiffness matrix of beam elements. The stiffness matrix of the beam element reads:

$$[K] = \begin{bmatrix} \frac{AE}{l} & 0 & 0 & 0 & 0 & 0 & -\frac{AE}{l} & 0 & 0 & 0 & 0 & 0 \\ & \frac{12EI_z}{l^3} & 0 & 0 & 0 & \frac{6EI_z}{l^2} & 0 & -\frac{12EI_z}{l^3} & 0 & 0 & 0 & \frac{6EI_z}{l^2} \\ & & \frac{12EI_y}{l^3} & 0 & -\frac{6EI_y}{l^2} & 0 & 0 & 0 & -\frac{12EI_y}{l^3} & 0 & -\frac{6EI_y}{l^2} & 0 \\ & & & \frac{GJ}{l} & 0 & 0 & 0 & 0 & 0 & -\frac{GJ}{l} & 0 & 0 \\ & & & & \frac{4EI_y}{l} & 0 & 0 & 0 & \frac{6EI_y}{l^2} & 0 & \frac{2EI_y}{l} & 0 \\ & & & & & \frac{4EI_z}{l^2} & 0 & -\frac{6EI_z}{l^2} & 0 & 0 & 0 & \frac{2EI_z}{l} \\ & & & & & & \frac{AE}{l} & 0 & 0 & 0 & 0 & 0 \\ & & & & & & & \frac{12EI_z}{l^3} & 0 & 0 & 0 & -\frac{6EI_z}{l^2} \\ & & & & & & & & \frac{12EI_y}{l^3} & 0 & \frac{6EI_y}{l^2} & 0 \\ & & & & & & & & & \frac{GJ}{l} & 0 & 0 \\ & & & & & & & & & & \frac{4EI_y}{l} & 0 \\ Sym & & & & & & & & & & & \frac{4EI_z}{l} \end{bmatrix} \tag{18}$$

To apply damping to the system, proportional or Rayleigh damping is used. It is assumed that the matrix of damping is proportional to a linear combination of mass and stiffness:

$$[C] = c_1[M] + c_2[K] \tag{19}$$

Where 'c_1' and 'c_2' are constant coefficients which show the effect of mass and stiffness on damping. The values of c_1 and c_2 are 400 and 4×10^7 as used by Naeimi et al. [17] .

As Figure 5. shows, sleepers are modeled as rigid bodies. Rail is linked to sleepers by rail pads modeled by linear spring and dashpots. Although previous studies showed that rail fastening behavior is not linear but an average value of stiffness produces good results [18]. Ballast material is considered to be rigid body which is connected to the subgrade. Since ballast is coarse aggregate material, the shear stiffness and damping or the effects of the interlocking ballast granules is also considered in modeling.

To find the effective mass and stiffness of ballast material, it is assumed that sleeper load distributes in conical area in ballast. The mass and stiffness of ballast will be calculated considering ballast in the cone area and the "outside ballast" is not considered in dynamic analysis. The so-called "ballast pyramid model" first developed by Ahlbeck et al [19]. In this paper, the pattern of load distribution in ballast was considered for non-overlapping pyramids of stress distribution in two neighboring sleepers. The equations proposed for mass and stiffness of the ballast for non-overlapping cones are [20-22]:

$$M_{bal} = \rho_{bal} h_{bal} \left[l_e l_{slp} + (l_e + l_{slp}) h_{bal} \tan\theta + \frac{4}{3} {h_{bal}}^2 \tan^2\theta \right] \tag{20}$$

$$K_{bal} = \frac{2(l_e - l_{slp}) \tan\theta}{ln\left[\left(\frac{l_e}{l_{slp}}\right).(l_{slp} + 2h_{bal}\tan\theta)/(l_e + 2h_{bal}\tan\theta)\right]} E_{bal} \tag{21}$$

Where ρ_{bal} stands for the density of the ballast, E_{bal} is the elastic modulus of ballast and h_{bal} represents the thickness of the ballast layer. l_e indicates the effective support range of a half sleeper, l_{slp} is the width of sleeper and θ shows the ballast stress distribution angle. Figure 5. depicts the effective volume of ballast used in ballast pyramid model [20].

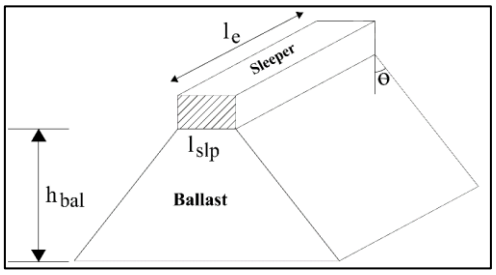

Figure 5. Stress Distribution in Ballast

The interaction matrix of track subsystem consisting rail, sleeper and ballast can be written as:

$$[I] = \begin{bmatrix} R & R/S & 0 \\ S/R & S & S/B \\ 0 & B/S & B \end{bmatrix} \tag{22}$$

R, S and B represent the matrices of mass, stiffness or damping for rail, sleeper and ballast respectively. Non-diagonal members represent the interaction between elements.

By the assemblage of the mass, stiffness and damping matrices of the track components, the dynamic equation of the track subsystem is presented in the following format.

$$[M^{tr}]\{\ddot{U}^{tr}\} + [C^{tr}]\{\dot{U}^{tr}\} + [K]\{U^{tr}\} = \{P^{tr}\} \tag{23}$$

The subscript 'tr' represents each matrix is formed by assembling track components matrices.

6. Solution to Train-Track Model

By the assemblage of the mass, stiffness and damping matrices of the vehicle and track elements, the dynamic equation of the whole system will be formed:

$$[M^t]\{\ddot{U}^t\} + [C^t]\{\dot{U}^t\} + [K^t]\{U^t\} = \{P(x,t)\} \tag{24}$$

Where, $[M^t]$, $[C^t]$ and $[K^t]$ are the matrices representing mass, damping and the stiffness of total train- track coupling system, respectively. P indicates the vector of load induced by the passage of the train.

To solve the dynamic equation of motion, Newmark integration method is used. This method, developed by Newmark (1959), is based on the assumption that the acceleration varies linearly between two instants of time. So if the track response is known at time "t", the response at time "t+dt" can be determined.

$$\{U_{t+dt}\} = [\bar{K}]\left[\{F_{t+dt}\} + [M]\left(b_1\{U_t\} + b_3\{\dot{U}_t\} + b_4\{\ddot{U}_t\}\right) + [C]\left(b_2\{U_t\} + b_5\{\dot{U}_t\} + b_6\{\ddot{U}_t\}\right)\right]$$
$$\{\dot{U}_{t+dt}\} = b_2(\{U_{t+dt}\} - \{U_t\}) - b_5\{\dot{U}_t\} - b_6\{\ddot{U}_t\} \quad (25)$$
$$\{\ddot{U}_{t+dt}\} = b_1(\{U_{t+dt}\} - \{U_t\}) - b_3\{\dot{U}_t\} - b_4\{\ddot{U}_t\}$$

Where $[\bar{K}] = (b_1[M] + b_2[C] + [K])^{-1}$ and b_1 to b_6 are constants [16]. Note that the value of dt =0.0001 is used as time step in numerical analyses.

Table 2. Track Parameters

Notation	Parameter	Value	Unit
M_r	Rail Mass Per Unit Length	60	Kg/m
M_{slp}	Sleeper Mass	250	Kg
l_s	Sleeper spacing	0.6	m
l_e	Effective support length of half sleeper	0.95	m
l_{slp}	Sleeper width	0.27	m
K_{pad}	Rail Pad Stiffness	4×10^7	N/m
C_{pad}	Rail pad Damping	1.3×10^5	N.s/m
h_{bal}	Ballast thickness	0.45	m
E_{bal}	Elastic Modulus of Ballast	1×10^8	N/m^2
K_{int}	Ballast Shear Stiffness	7.8×10^7	N/m
C_{int}	Ballast Shear Damping	8×10^4	N.s/m
θ	Ballast stress distribution angle	35	degree
C_{bal}	Ballast Damping	8×10^4	N.s/m
E_{sub}	Elastic Modulus of Subgrade	8×10^7	N/m^2
C_{sub}	Subgrade Damping	5.5×10^4	N.s/m
$K_{w/r}$	Hertz Spring Constant	1.1×10^{11}	$N/m^{3/2}$
R_{rail}	Rail head radius	0.3	m

7. Track Model validation

To show the validity of the numerical solution and formulation procedure, the response of a beam under a series of moving loads from current solution were compared with the results from theoretical solutions for the same problem. 0. shows a series of concentrated loads on an Euler-Bernoulli beam as a validation model. The beam is rested on elastic foundation and track stiffness and damping have been modeled by a continuous layer of springs with stiffness K_p and dampers with constant C_p in unit length. The loads are moving at speed "v".

Using the above assumptions, the governing differential equations of beam on elastic foundation can be determined [23]:

$$EI_r \frac{\partial^4 w_r(x,t)}{\partial x^4} + m_r \frac{\partial^2 w_r(x,t)}{\partial t^2} + k_p w_r(x,t) + c_p \frac{\partial w_r(x,t)}{\partial t} = P_0 \exp(i\bar{\omega}t)\delta(x - vt) \quad (26)$$

Where $\delta(x-vt)$ is Dirac delta function and $w_r(x,t)$ and $\bar{\omega}$ indicate rail displacement and load frequency. Terms $exp(i\bar{\omega}t)$ and $\delta(x-vt)$ respectively show that the load is oscillating with frequency $\bar{\omega}$ and moving. It is also assumed that at time t=0, the location of first load is x=0.

A number of solutions proposed to solve the differential equation [23, 24]. An easy way to solve the above differential equation is to use Fourier transformation. In other words, the problem should be transformed from time-space domain (x, t) to wavenumber-frequency domain (ζ , ω).

Double Fourier transform results in

$$EI_r\zeta^4\tilde{w}_r - m_r\omega^2\tilde{w}_r + k_p\tilde{w}_r + c_p i\omega\tilde{w}_r = 2P_0\pi\delta(\omega + \zeta v - \tilde{\omega}) \quad (27)$$

In which $\tilde{w}_r$ and $\tilde{\omega}$ are transformed rail displacement and load frequency respectively, and "i" is unit imaginary number.

Applying double inverse Fourier Transform, Rail displacement in time-space domain take form:

$$w_r(x,t)=\frac{P_0\exp(i\bar{\omega}t)}{2\pi}\int_{-\infty}^{\infty}\frac{\exp\left(i\zeta\left(x-vt\right)\right)}{EI_r-m\bar{\omega}^2-mk^2V^2+2mkV\bar{\omega}+k_p+\bar{\omega}c_pi-k_pc_pVi}d\zeta \quad (28)$$

By determining the poles of the function and applying theory of residues, rail displacement can be determined [23]. The solution can be repeated for other three loads which are located at 2, 8 and 10 meters from the first load. Assuming linear elastic materials, beam response can be calculated by superposition principle.

0Figure 7. shows the time histories of midpoint deflection obtained by the current and analytical solutions. As the Figure suggests, the results from numerical procedure used in this paper are in good agreement with those from theory. In the graph, less than 5% discrepancy can be observed. Note that no rail irregularities are considered in the verification model, and the loads are assumed to be non-oscillating and constant. The parameters used in both theoretical and numerical solutions are shown in Table 3.

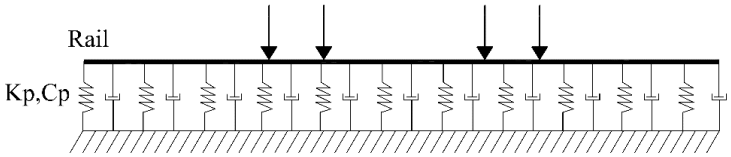

Figure 6. Euler-Bernoulli beam on elastic foundation

Table 3. Parameters of validation model

Notation	Parameter	Value	Unit
F	Wheel-set load	15	ton
K_p	Rail support stiffness	2×10^6	N/m
C_p	Rail support damping	25000	N.s/m
v	Moving loads' speed	20	m/s
l	Length of rail	36	m
E	Rail's elsatic modulus	2×10^{11}	N/m^2
I_r	Rail's moment of inertia	3×10^{-5}	m^4
m	Beam mass of a unit length	50	Kg/m

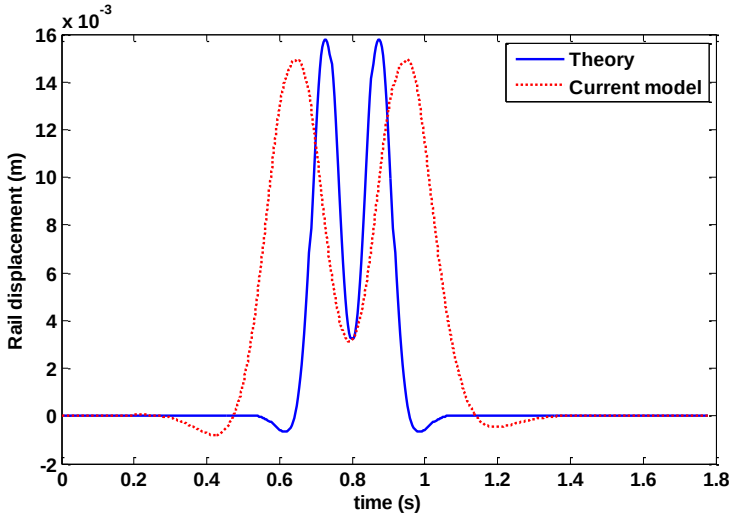

Figure 7. Rail midpoint displacements from theory and current model

8. Results of numerical analysis

This paper investigates the effect of rail defects on track and vehicle response. Three kinds of rail flaws are considered; rail irregularities, rail joints (with or without dip and raise) and rail corrugation. The results obtained for

different parameters to determine the significance of rail flaws on rail impact factor. In the analyses, unless mentioned otherwise, it is assumed that track is in class 6 condition and train speed is 100 km/hr.

8.1. Effect of Rail Corrugation

Corrugation is a prevalent defect on rail head initiating from rail head de-carbonization (on new steel) and irregularities such as; rail manufacture pitting, contact fatigue defects, rail welds, rail joints, etc. [25] corrugation with different depth and frequency can be detected in the field. International Union of Railways based on wavelength divided this defects into two groups: short-pitch with wavelength between 3 to 8 cm and long-pitch corrugation with wave length between 8 to 30 cm [26]. The depth of corrugation also varies depending on rail and wheel condition. In this study, the depth of corrugation considered between 0.01 to 0.1 mm. Figure 8. shows the short (0.05 m wavelength) and long pitch (0.3 m wavelength) corrugation. The corrugation is simulated as a sine wave and the same phase for the right and left rails.

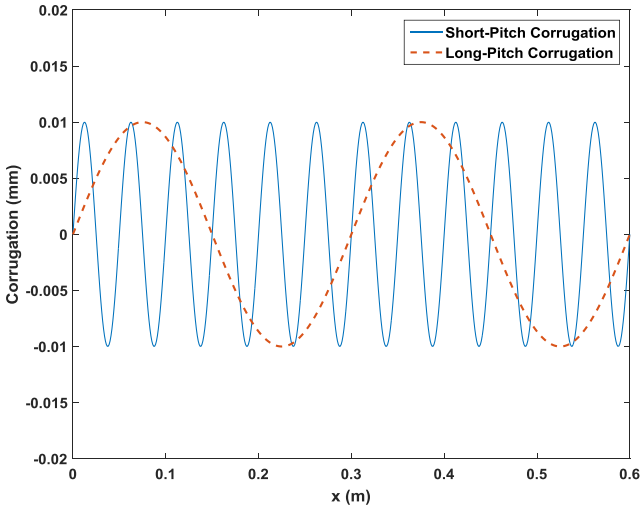

Figure 8. Short-pitch and long-pitch corrugation

To demonstrate the effect of rail defects on dynamic forces, impact factor will be used as a criterion. Impact Factor which indicates the increase in forces due to dynamics effects is defined in the following equation

$$\text{Impact Factor}(\%) = \frac{\text{Maximum Dynamic Responce} - \text{Maximum Static Response}}{\text{Maximum Static Responce}} \times 100 \quad (29)$$

It should be noted that based on the vehicle data used in this paper, the static load of train is 75 KN. Figure 9. shows the effect of rail corrugation depth and wavelength on rail displacements. Increasing corrugation depth from 0.02 mm to 0.05 mm leads to 0.1 mm increase in rail vertical displacement. But corrugation wavelength is not as effective as depth and the maximum rail displacement in this case is about 0.05 mm.

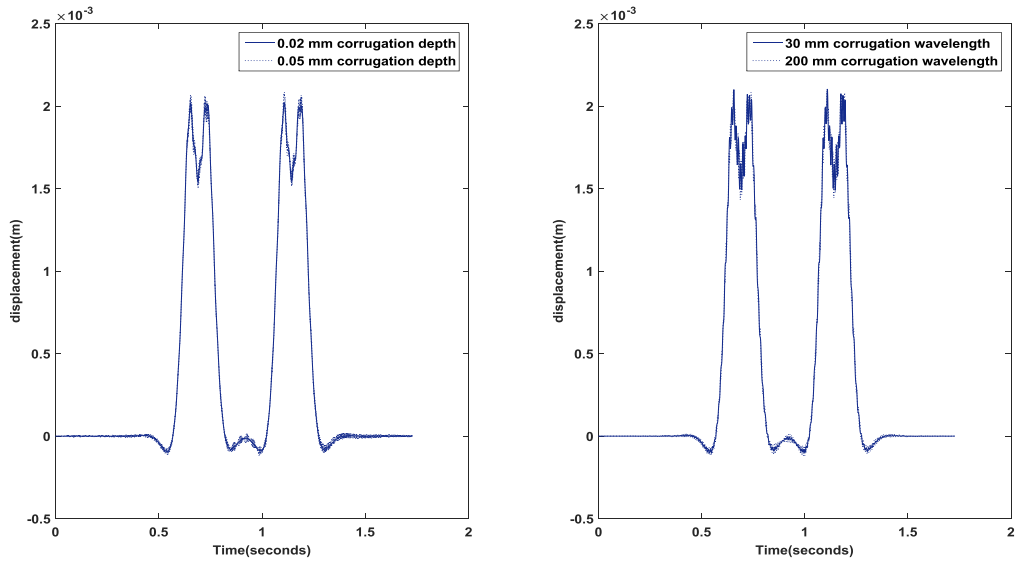

Figure 9. Effect of rail corrugation depth (left) and rail corrugation wavelength (right) on rail displacement

Figure 10. shows the relation between corrugation depth and the impact factor of the rail and vehicle forces. It is evident that for deeper corrugation, the accelerated increase of impact factor occurs. The same trend can be observed for rail, primary suspension and car body. The highest rail IF is 103% for 0.1 mm rail corrugation.

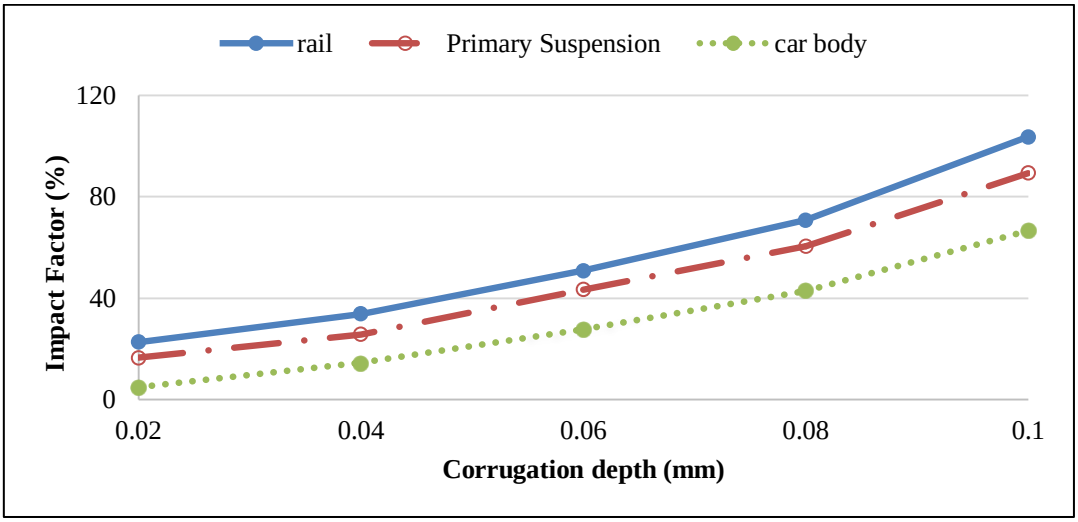

Figure 10. The effect of corrugation depth on rail impact factor

Figure 11. shows the impact factor for different corrugation wavelength. In this case, the depth of corrugation is 0.04 mm and the dynamics amplification is observed for different wavelength range from 50 to 300 mm. The Figure shows that with increasing wavelength impact factor decreases considerably. This trend is valid especially for lower wavelengths. As the wavelength of corrugation increases the rate of IF reduction drops. This trend can be clearly seen in case of car body vertical force IF where the graph consists of three parts and IF decreases sharply as wavelength increases.

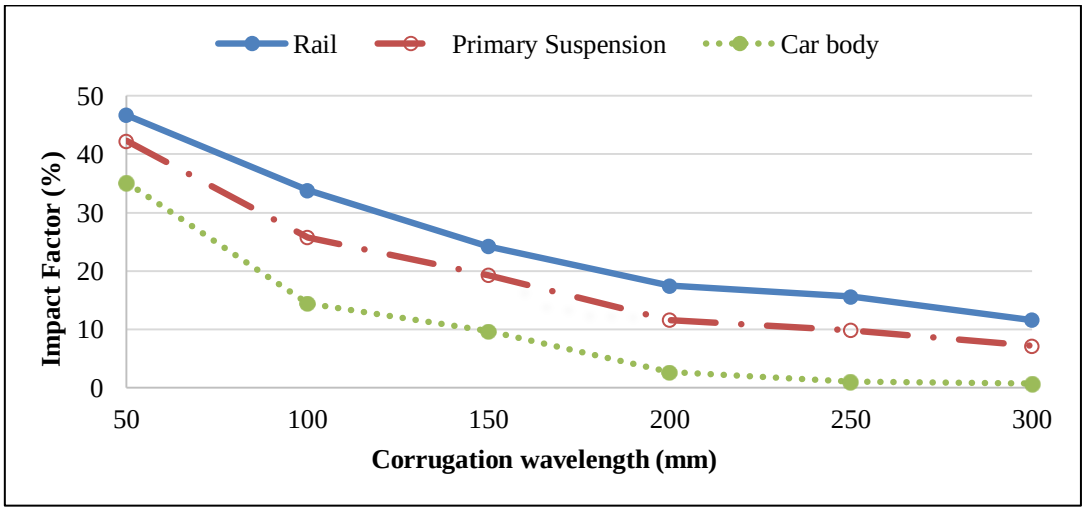

Figure 11. the effect of corrugation wavelength on rail impact factor

Figure 12. and 13. demonstrate the effect of train speed on rail IF for different wavelengths and depths. As Figure 12. depicts, at a certain speed the dynamic force reaches its maximum value. This critical speed for wavelength 100 and 200 mm is 200 km/hr. and for corrugation with wavelength 300 mm increases to about 250km/hr. It is evident from Figure 13. that there is the same trend for deeper corrugation but in this case, the IF increases substantially and the maximum IF is 4.7 times greater than that of 0.01 mm corrugation depth. This graph also shows that increasing corrugation depth has a major effect on rail IF for longer wavelength. For example, in case of 250 km/hr train speed shown in Figure 12, the IF corresponding to 300 mm wavelength is 4% higher than that of 100 mm wavelength while as shown in Figure 13, this value increases to 31% with increasing corrugation depth from 0.01 to 0.1 mm.

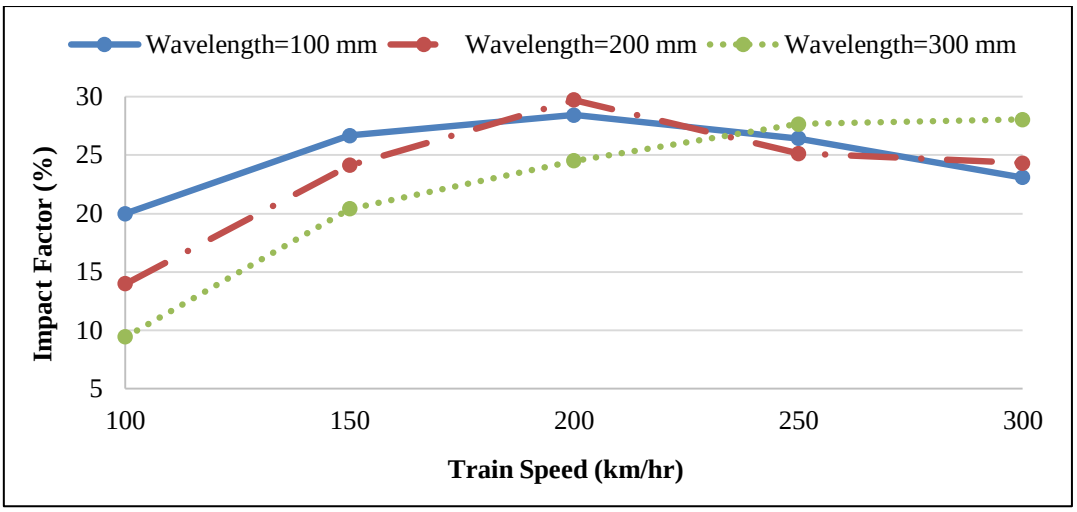

Figure 12. the effect of train speed on rail impact factor (for 0.01 mm corrugation depth)

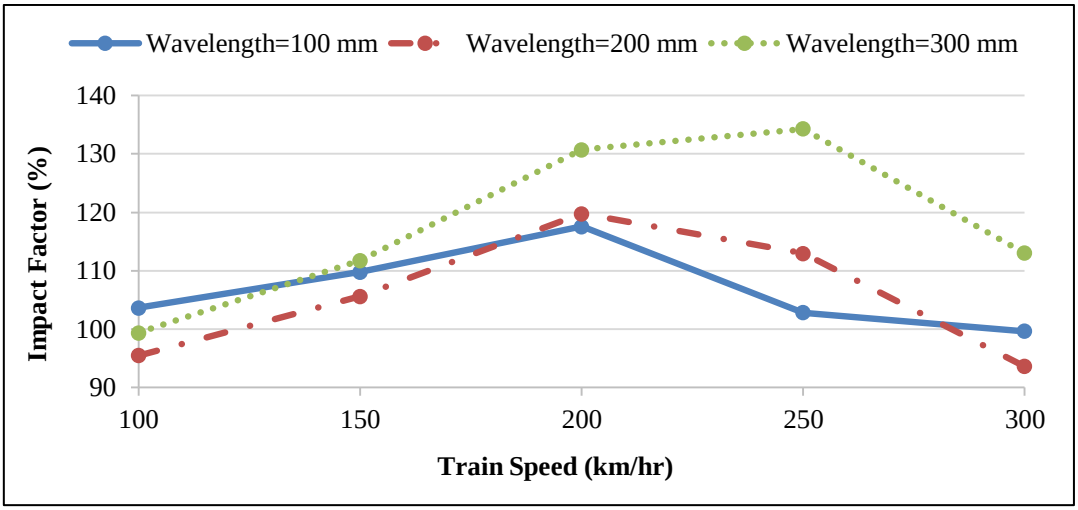

Figure 13. the effect of train speed on rail impact factor(for 0.1 mm corrugation depth)

8.2. Rail joint dip and raise

Some rail defects including shelling of running surface, crushing and rail burning may cause rail dip. Many of these defects are not visible or hardly visible at the outset, and become apparent in the track after a time-interval which varies according to the traffic load [26]. Rail joints are one of the most important track points of weakness. Due to defects such as dip angle and height difference, rail joints are susceptible to cause rail accidents. This problem specially arises when the rail joint is dipped. Figure 14. shows a schematic view of rail dip. The curve of the dipped rail is modeled by quadratic functions and characterized by parameters "L", length of dip and "α", the dip angle [9].

The opposite case or raise on rail joints may also happen. This flaw may especially occurs due to manufacturing or material defects and improper welding [6, 27]. Raise on rail surface is a dangerous defect and generates great dynamic forces. In order to compare the results from rail surface flaws, the same conditions as rail dip has been taken into account. The shape of raise on rail surface is quadratic and the same parameters "L" and "α" have been used to characterize the rail defect.

In this paper, the effect of rail defect parameters on rail impact factor is investigated for track class 6 and different train speeds. The rail joint defects are assumed at the same phase for the right and left rails.

Figure 15. shows the rail impact factor in rail joint with and without defect for different train speed. As the Figure suggests, in case of no defect condition, the impact factor does not change considerably with increasing load speed. The maximum impact factor is 13% for 100 km/hr train speed. However, dip in rail joint has a profound influence on rail dynamic forces. With increasing speed, impact factor increases from 18% to 62% when vehicle speed increases from 50 to 200 km/hr. the graph also demonstrates that the rate of increase in impact factor is a function of train speed and higher speeds result in increasingly more impact factor. Figure 15. to 17. also compares rail impact factor for rail joint raise and dip. The results of the study shows the defects causing rail raise generally produce much more dynamic

forces compared to dip type defects. Figure 16. implies that the rail impact factor increases considerable when the depth of defect increases. In Figure 17, with increasing the defect length, the rail impact factor increases sharply to the maximum value which occurs at the defect length of 0.3 m, then it decreases. This Figure also shows that the effect of the defect length on the rail impact factor reduces gradually. Moreover, it is evident that for the shorter defect length, the difference of rail impact factors between raised and dipped flaw is considerable.

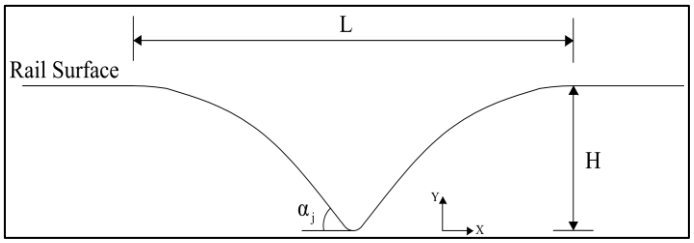

Figure 14. Rail dip shape

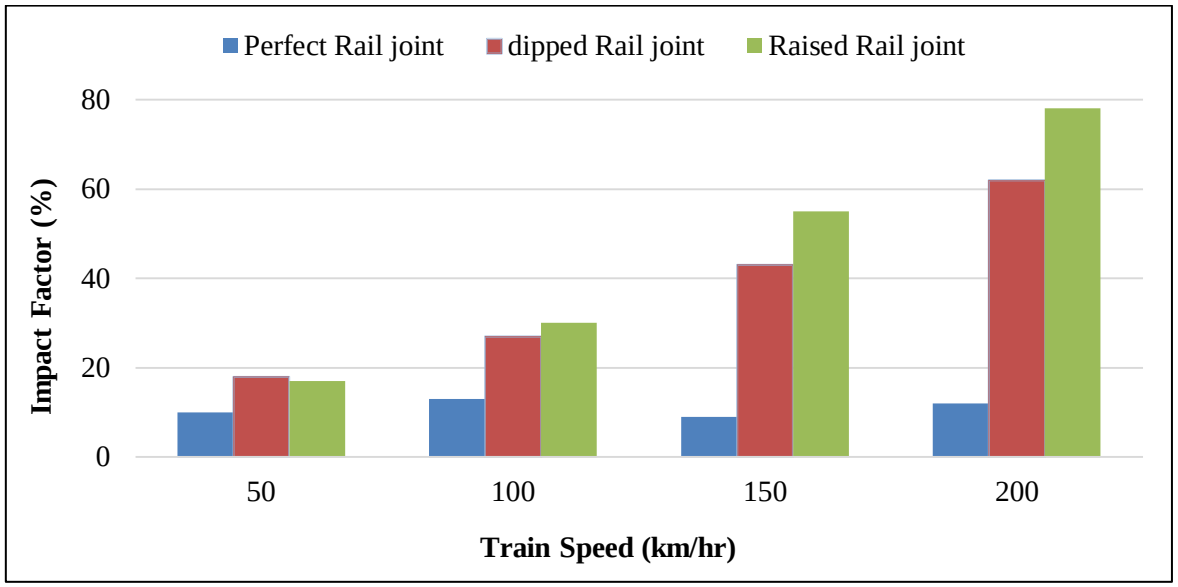

Figure 15. The effect of dip and raise on rail joint impact factor

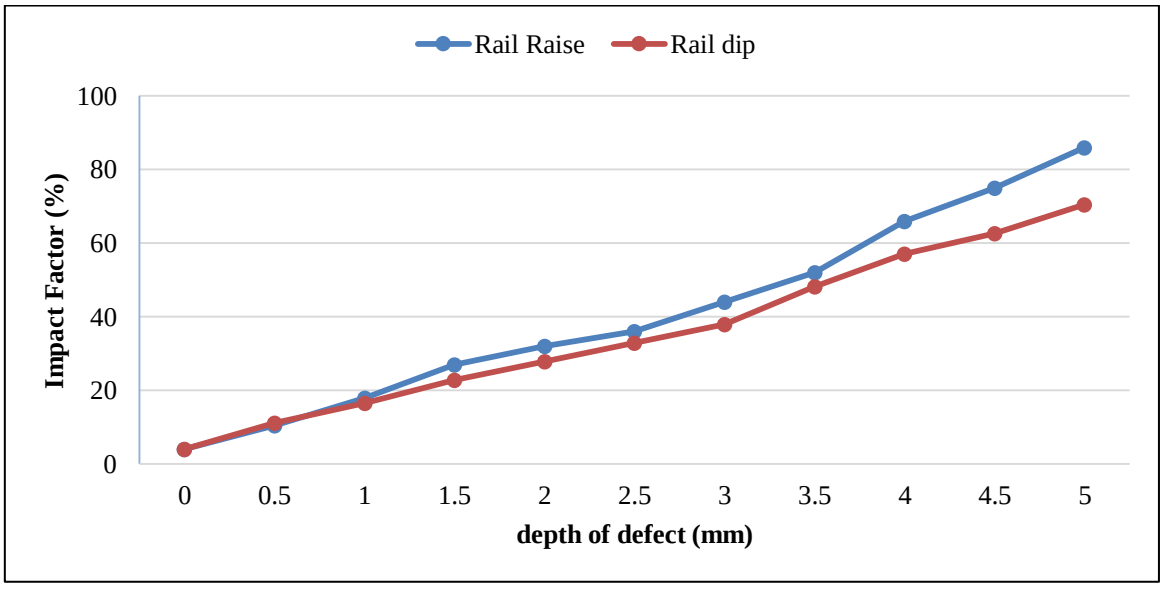

Figure 16. The effect of depth of rail dip and raise on rail impact factor

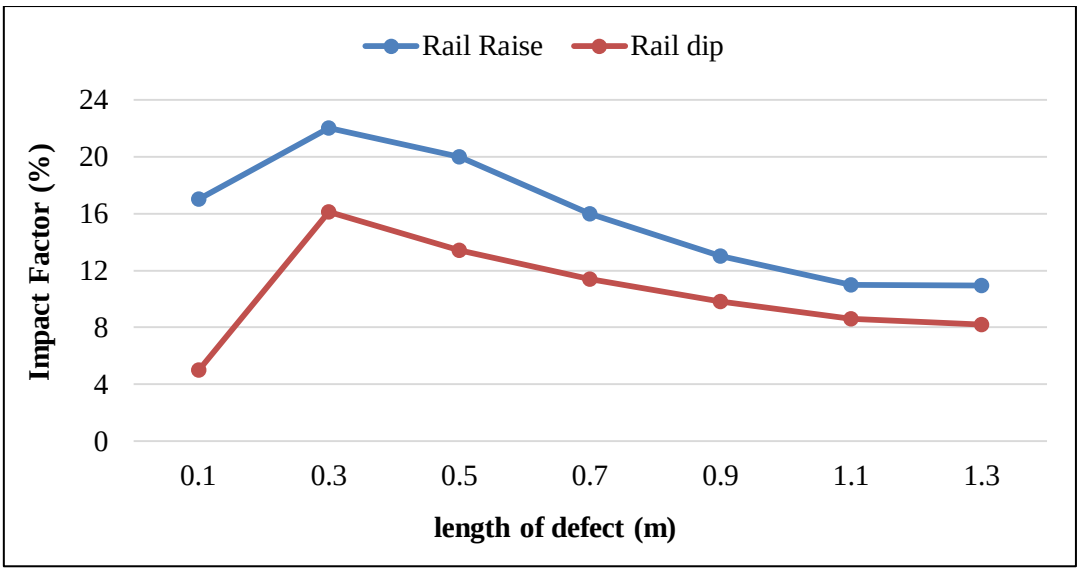

Figure 17. the effect of the length of rail dip and raise on rail impact factor

8.3. Rail random irregularities

As mentioned earlier, track irregularities have random nature and no specific pattern can be seen. As a result no detectable trend in impact factor can be observed. Figure 18. And 19. show the impact factor of rail, primary suspension and car body for different train speeds for tracks class 4 and 6 respectively as defined by FRA. Comparison of the results obtained from class 6 track with those of class 4 track reveals that improving track condition leads to about 25% reduction in rail impact factor. But in case of car body, the difference between impact factors obtained from class 4 and 6 limited to 17%. It is also evident that the train speed has little influence on IF when that increases to 250 km/hr or higher.

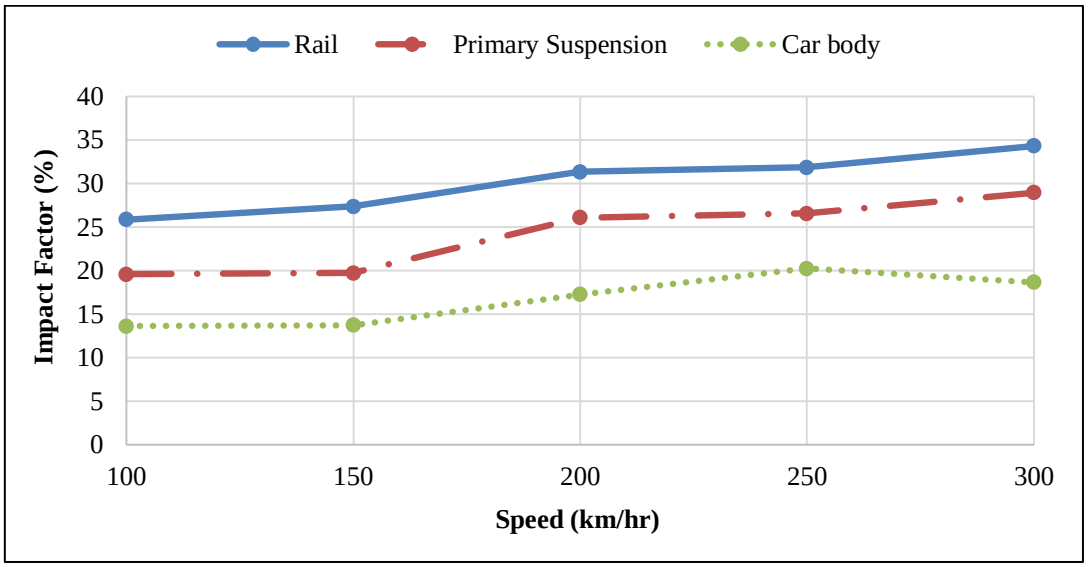

Figure 18. Rail impact factor for class 6 track

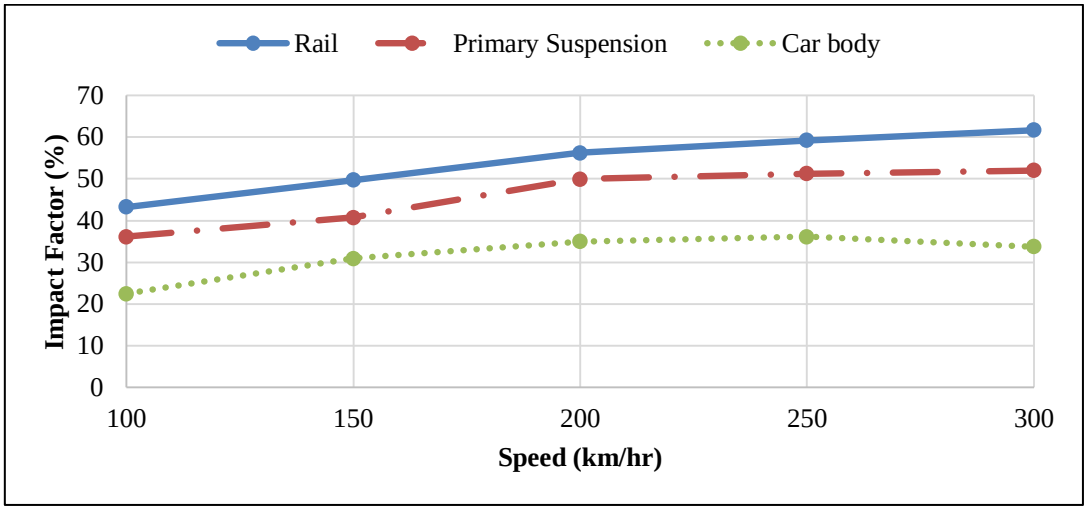

Figure 19. Rail impact factor for class 4 track

9. Conclusion

This paper investigated the effect of rail surface defects on dynamic loads. To obtain the accurate results, a three-dimensional vehicle-track model considering wheel-rail interaction developed and soled in time domain using Newmark integration method. The model is able to simulate vertical as well as lateral displacements of vehicle and track. The model was used to determine the impact factor from three rail flaws; rail corrugation, rail random irregularities and dip at rail joints. The numerical results made the following conclusions

- Joint in railroad track causes an increase in rail impact factor but in case of no defects, the train speed does not have considerable influence on rail impact factor. However, dip or raise in rail joint has a great influence on dynamic forces. For dipped rail, with increasing speed, impact factor increases from 18% to 62% when vehicle speed increases from 50 to 200 km/hr.
- The depth and length of the rail joint raise or dip are important factors on dynamic forces from railroad vehicle. The results of the study indicate that for defect length shorter than 0.3 m there is a large difference of the impact factors between rail joint dip and raise but with increasing the defect length, the difference decreases.
- Corrugation has the biggest influence on rail impact factor. Based on the results of the study, increasing corrugation depth generates a large impact factor. As it is expected, shorter wavelength causes greater impact factor.
- Rail random irregularities significantly affect rail dynamic forces. The amount of dynamic forces is a function of track quality and train speed. The impact factor generated from track class 4 is much larger than that due to track class 6, especially for high-speed trains. The results show that increasing vehicle speed does not necessarily increase impact factor. It is especially valid for bogie and car body impact factor that the impact factor reduces when the train speed increases to 250 km/hr or higher.

10. References

[1] X. Liu, M. R. Saat, and C. P. L. Barkan, "Analysis of causes of major train derailment and their effect on accident rates," Transp. Res. Rec., vol. 2289, no. 2289, pp. 154–163, 2012.

[2] L. Frýba, Dynamics of Railway Bridges, 2nd ed. Academia Praha, 1996.

[3] S. L. Grassie, "Rail corrugation: Characteristics, causes, and treatments," Proc. Inst. Mech. Eng. Part F J. Rail Rapid Transit, vol. 223, no. 6, pp. 581–596, 2009.

[4] Y. Sato, A. Matsumoto, and K. Knothe, "Review on rail corrugation studies," Wear, vol. 253, no. 1–2, pp. 130–139, 2002.

[5] J. Sadeghi and M. Fesharaki, "Importnace of Nonlinearity of Track Support System in Modeling of Railway Track Dynamics," Int. J. Struct. Stab. Dyn., vol. 13, no. 1, p. 16, 2013.

[6] Y. Q. Sun and M. Dhanasekar, "A dynamic model for the vertical interaction of the rail track and wagon system," Int. J. Solids Struct., vol. 39, no. 5, pp. 1337–1359, 2002.

[7] E. Kabo, J. C. O. Nielsen, and a. Ekberg, "Prediction of dynamic train–track interaction and subsequent material deterioration in the presence of insulated rail joints," Veh. Syst. Dyn., vol. 44, no. sup1, pp. 718–729, 2006.

[8] Y. Q. Sun, C. Cole, and M. Spiryagin, "Study on track dynamic forces due to rail short-wavelength dip defects using rail vehicle-track dynamics simulations," J. Mech. Sci. Technol., vol. 27, no. 3, pp. 629–640, 2013.

[9] T. X. Wu and D. J. Thompson, "On the impact noise generation due to a wheel passing over rail joints," J. Sound Vib., vol. 267, no. 3, pp. 485–496, 2003.

[10] X. S. Jin, Z. F. Wen, K. Y. Wang, Z. R. Zhou, Q. Y. Liu, and C. H. Li, "Three-dimensional train-track model for study of rail corrugation," J. Sound Vib., vol. 293, no. 3–5, pp. 830–855, 2006.

[11] V. N. Dinh, K. Du Kim, and P. Warnitchai, "Dynamic analysis of three-dimensional bridge-high-speed train interactions using a wheel-rail contact model," Eng. Struct., vol. 31, no. 12, pp. 3090–3106, 2009.

[12] C. Esveld, Modern Railway Track , 2nd ed. MRT Productions, 2001.

[13] A. Hamid, K. Rasmussen, M. Baluja, and T.-L. Yang, "Analytical Descriptions of Track Geometry Variations," Springfield, VA, 1983.

[14] T.-L. Wang, "Impact and Fatigue in Open Deck Steel Truss and Ballasted Prestressed Concrete Railway Bridges," PhD dissertation, Illinois Institute of Technology, 1984.

[15] Y.C.Yang, Random vibration of structures, 1st ed. John Willey & Sons, 1986.

[16] A. K. Chopra, Dynamics of Structures, 4th ed. Prentice-Hall, 2011.

[17] M. Naeimi, J. A. Zakeri, M. Esmaeili, and M. Mehrali, "Influence of uneven rail irregularities on the dynamic response of the railway track using a three-dimensional model of the vehicle–track system," Veh. Syst. Dyn., vol. 53, no. 1, pp. 88–111, 2015.

[18] J. Sadegi, M. Fesharaki, and Amin Khajehdezfuly, "Influences of Train Speed and Axle loads on Life Cycle of Rail Fastening Clips," Transactions of the Canadian Society for Mechanical Engineering, Vol. 39, no. 1, 2015

[19] D. R. Ahlbeck, H. C. Meacham, and R. H. Prause, "The development of analytical models for railroad track dynamics," in Railroad Track Mechanics & Technology, A. D. Kerr, Ed. Oxford: Pergamon Press, 1978.

[20] W. M. Zhai, K. Y. Wang, and J. H. Lin, "Modelling and experiment of railway ballast vibrations," J. Sound Vib., vol. 270, no. 4–5, pp. 673–683, 2004.

[21] Y. Yang, J. Yau, and Y. Wu, Vehicle-bridge interaction dynamics with applications to high-speed railways. World Scientific, 2004.

[22] M. Esmaeili, J. Sadeghi, and M. Fesharaki, "Vehicle dynamic interaction with railway track embankment," Proc. Inst. Civ. Eng. - Transp., vol. 167, no. 1, pp. 15–26, 2014.

[23] M. F. M. Hussein and H. E. M. Hunt, "Modelling of floating-slab tracks with continuous slabs under oscillating moving loads," J. Sound Vib., vol. 297, no. 1–2, pp. 37–54, 2006.

[24] L. Frýba, Vibratiob of Solid and Structures under Moving Loads. Thomas Telford, 1999.

[25] American Railway Engineering and Maintenance-of-Way Association, Manual for Railway Engineering, Vol.1, Track. 2010.

[26] International Union of Railways, "Rail defects, UIC code 712R," 2002.

[27] M. J. M. M. Steenbergen and C. Esveld, "Relation between the geometry of rail welds and the dynamic wheel - rail response: numerical simulations for measured welds," Proc. Inst. Mech. Eng. Part F J. Rail Rapid Transit, vol. 220, no. 4, pp. 409–423, 2006.